ELSEVIER

Microstructural evolution in spray-formed and melt-spun $Al_{85}Nd_5Ni_{10}$ bulk hybrid composites

M.L. Ted Guo [a], Chi Y.A. Tsao [a,*], J.C. Huang [b], J.S.C. Jang [c]

[a] Department of Materials Science and Engineering, National Cheng Kung University, 1, Da-Shieh Road, 70101 Tainan, Taiwan, ROC
[b] Institute of Materials Science and Engineering, National Sun Yat-Sen University, 70 Lien-hai Road, 804 Kaohsiung, Taiwan, ROC
[c] Department of Materials Science and Engineering, I-Shou University, 1, Section 1, Hsueh-Cheng Road, Ta-Hsu Hsiang, Kaohsiung County, 840 Taiwan, ROC

Available online 9 March 2006

Abstract

Microstructure evolutions in the spray-formed and melt-spun $Al_{85}Nd_5Ni_{10}$ alloys were studied. The spray forming process has shown to be capable of directly producing a bulk scale $Al_{85}Nd_5Ni_{10}$ hybrid composite consisting of amorphous and nanostructured phases without the need of using an amorphous precursor. The spray-formed overspray flakes were partially amorphous, and the amorphous phase came from the undercooled liquid droplets upon deposition. The as-spray-formed deposit was completely crystallized due to the devitrification of the retained amorphous phase to nanoscale secondary crystals upon deposition. In the deposit and flake, the primary crystals were micro-scaled Al_6NdNi_2, and the secondary crystals devitrified from the amorphous phase during spray forming process were nanoscaled Al_3Ni and Al_6NdNi_2, dispersed in nanoscaled α-Al matrix. The completely devitrified melt-spun ribbon composite consisted of secondary crystals Al_3Ni, $Al_{11}Nd_3$ and Al_6NdNi_2 with nanoscale sizes, dispersed in the nanoscaled α-Al matrix. Deformation twins were observed in the primary Al_6NdNi_2 crystal in the as-spray-formed flake and deposit, but were not found in the secondary Al_6NdNi_2 crystals in the completely devitrified ribbon.
© 2006 Elsevier Ltd. All rights reserved.

Keywords: A. Composites; A. Nanostructured intermetallics; B. Twinning; C. Rapid solidification processing; F. Electron microscopy, transmission

1. Introduction

Since 1988 [1–5], many Aluminum–Rare Earth–Transition Metal (Al–RE–TM) composites with ultra-high strength (> 1 GPa) have been developed from annealing the amorphous precursors [6,7]. The uniformly dispersed α-Al crystals in the amorphous matrix can retard the movement of shear bands during deformation and further increase the strength. However, synthesizing an amorphous Al–RE–TM precursor requires a very high cooling rate. Therefore, melt-spinning technique is by far the most preferred method to make the amorphous precursors. Subsequent to the melt-spinning step, many secondary processes, such as warm extruding and hot pressing can be used to consolidate the melt-spun ribbons into a bulk amorphous sample.

In this study, spray forming process was employed to fabricate an Al–RE–TM hybrid composite, consisting of amorphous and nanostructured phases, in one step without precursor. Spray forming [8–11] is a rapid solidification process in which the molten metal are atomized into fine droplets by high pressure nitrogen gas and then collected into a dense deposit on the substrate after a short flight distance. Its most attractive features are the ability to create refined microstructure and reduced segregation [12]. An Al–10Ni–5Mm (Misch metal) amorphous sheet (7 mm in thickness and 50 mm in length) was produced by a spray forming process [13]. A spray-formed Al–8Y–5Ni–2Co (2 kg) composite [14] produced under an increased gas/metal ratio (G/M ratio, 10 m^3/kg) resulted in 76% amorphous phase. An Al–3Y–8Ni–4Co–1Zr (7 kg) hybrid composite [15], spray-formed at a somewhat lower G/M ratio (8.7 m^3/kg) was fully crystallized. These previous studies concluded that the crystallization of spray-formed materials was caused by heat accumulation during the deposition. In this study, a liquid nitrogen (LN) cooled copper substrate was used during spray forming to increase the heat dissipation, anticipating to make a bulk hybrid composite consisting of both amorphous and crystalline phases.

The composition map for amorphous Al–Nd–Ni ribbon synthesis has been established by Inoue [16,17]. A high strength (>1 GPa) ribbon was produced at a relatively lower Nd content ($\sim$4%), as compared to the other rare earth elements (Y, La or Ce). While the solute contents (Nd + Ni) increase from 8% ($Al_{92}Nd_4Ni_4$) to 10% ($Al_{90}Nd_4Ni_6$), the resultant ribbon structure vary from 'amorphous plus α-Al' to

* Corresponding author. Tel./fax: +886 6 2083889.
E-mail address: tsao_cya@alum.mit.edu (C.Y.A. Tsao).

'brittle amorphous'. A subsequent increase in the solute content to 16% ($Al_{84}Nd_4Ni_{12}$) results in a 'ductile amorphous' structure in the ribbon. Recently, an Al–Nd–Ni ternary phase diagram was also established [18]. The composition of $Al_{85}Nd_5Ni_{10}$ was selected in this study to produce spray-formed hybrid composites. Melt-spun specimens were also produced for comparison. Microstructural evolutions in both spray-formed and melt-spun materials are discussed.

2. Experimental procedure

An aluminum–nickel master alloy was prepared by melting of the mixtures of aluminum ingot (99.8%+ Si and Fe) and some Al–80Ni flux, which was melted with Nd (99.9%) slug under nitrogen atmosphere in a graphite crucible with a totally weight of 5 kg. During spray forming, the molten metal was atomized by nitrogen gas into fine droplets, and deposited onto a liquid nitrogen (LN)-cooled copper substrate to form a deposit (230 mm in diameter and 30 mm in thickness), during which overspray flakes (15 mm in width and 1 mm in thickness) and overspray powders not deposited on the substrate were generated and collected. The weight of the deposit was about 2 kg. Some material cut from the spray-formed deposit was melt-spun on a copper wheel with a surface speed of 30 ms^{-1} under argon gas to form ribbons of 20–30 μm in thickness and 2–3 mm in width. The as-spray-formed deposit was designated as SD, as-spray-formed overspray flakes as SF, as-spray-formed powders as SP, and as-melt-spun ribbons as MS30.

The compositions of the alloys were measured by the inductively coupled plasma-mass spectrometry (ICP) method (Perkin–Elmer Optima 3200 RL). The X-ray (Cu Kα) diffraction tests (Rigaku geigerflex) were performed from angles of 20–80° at a scanning speed of 3°/min. Because the database [19] does not include the $Al_{11}Nd_3$ phase in this study, the information of an $Al_{11}La_3$ phase with an identical crystal structure (Orthorhombic Immm) was adopted to help determine the peak of $Al_{11}Nd_3$, which was called '$Al_{11}Nd_3$-like'.

Quantitative wave-length diffraction spectrum (WDS) analyses and back-scattered electron image (BEI) of the phases were carried out using a WD/ED combined microanalyzer (JEOL™ JXA-8900R). Samples were also investigated by a differential scanning calorimeter (DSC, Perkin–Elmer Pyris1) and differential thermal analyzer (Perkin–Elmer DTA7) to determine the reactions during heating. A transmission electron microscopy (TEM) (JEOL AEM3010) equipped with a nanovolume energy dispersive spectrometry (EDS) system was used. TEM samples
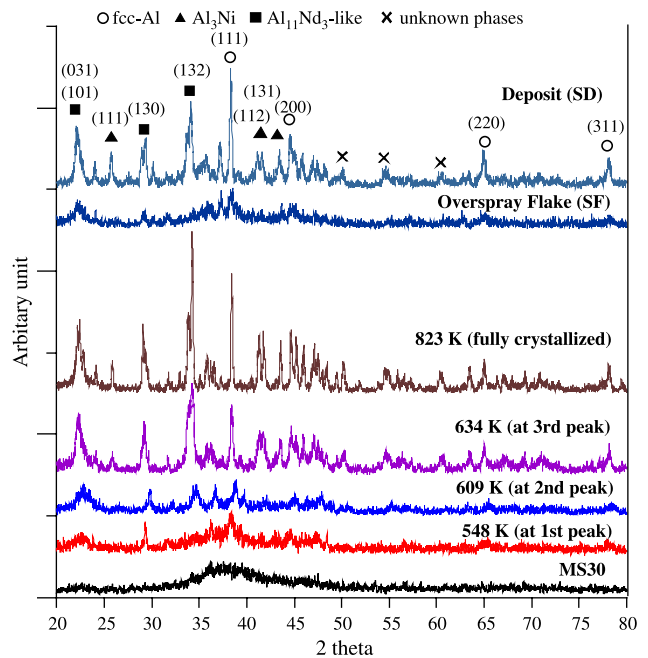

Fig. 1. XRD patterns from the SD, SF and MS30 samples, together with the MS30 heated in DSC to 548, 609, 634 and 823 K.

were prepared by ion milling (Gatan 691) with angles of 8–4° and with beam energy of 4.5 kV and 25 μA.

3. Results

Table 1 shows the chemical compositions of the SD, SF and MS30 determined by an ICP technique, which were quite close. Fig. 1 shows the XRD patterns of the SD, SF and MS30,

Table 1
Chemical compositions of the SD, SF and MS30

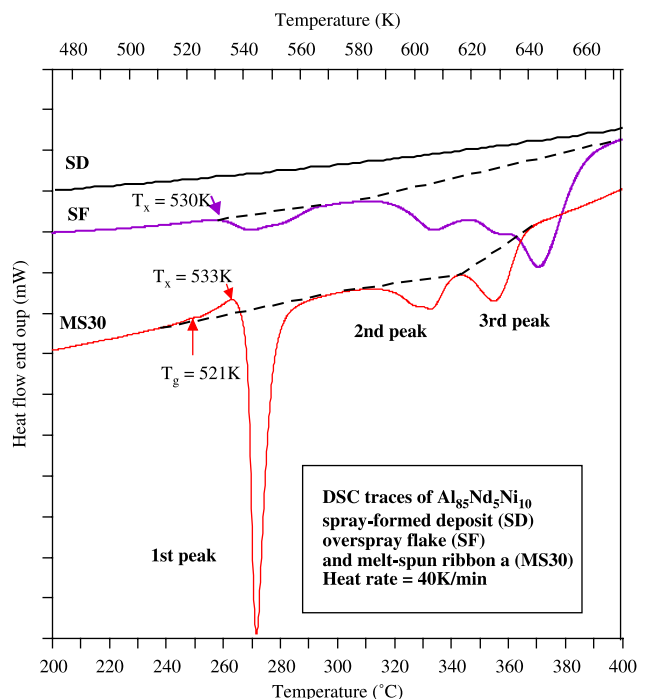| at.%	SD	SF	MS30
Al	84.8/84.8	84.9/84.7	85.1/84.9
Ni	10.6/10.6	10.6/10.7	10.4/10.6
Nd	4.6/4.6	4.5/4.6	4.5/4.5

Fig. 2. DSC traces from the SD, SF and MS30 samples, showing distinct crystallization stages.

Table 2
Crystallization stages and enthalpies released for the MS30 and SF during continuously heated to 823 K in DSC

		1st stage	2nd stage	3rd stage
MS30	Onset temperature (K)	533	587	610
	ΔH (J/g)	57.2	9.5	14.7
SF	Onset temperature (K)	530	581	
	ΔH (J/g)	4.1	47.2	

Heating rate = 40 K/min.

together with the patterns of the MS30 heated to various temperatures. The MS30 exhibits a typical amorphous halo peak, and the SF shows a quite similar pattern with the small characteristic peaks of the α-Al and $Al_{11}Nd_3$-like phases. The SD shows a completely crystallized pattern, consisting of the α-Al, Al_3Ni, $Al_{11}Nd_3$-like and some unknown phases. The completely devitrified MS30 shows a quite similar pattern as that for the SD.

Fig. 2 shows DSC traces of the SD, SF and MS30 continuously heated to 823 K at 40 K/min. The MS30 exhibits multi-exothermic reactions, which correspond to three devitrification stages with the peak temperatures of 548, 609 and 643 K, respectively. The SF shows overlapped exothermic reactions and a reduced exothermic enthalpy at first peak, which suggests that the SF is partially amorphous. The SD

shows nearly no exothermic reaction, indicating it is a fully crystallized structure.

Table 2 shows the crystallization stages and the enthalpies released for the MS30 and SF continuously heated to 823 K in DSC. Total enthalpy released from RT to 823 K for the MS30 is about 81.4 J/g, and the total enthalpy released for the SF is about 51.3 J/g. For the convenience of calculation, the MS30 was assumed to be a fully amorphous specimen (as a baseline of 100% amorphous), even though some quenched-in nuclei might exist in it. Therefore, the percentage of the amorphous phase of the SF is estimated to be 51.3/81.4 = 63% [20,21], while the other 37% is the crystalline phase.

Fig. 3 shows the micrographs of the back-scattered electron images (BEI) of the SD, SF, MS30 and SP. The rod-shaped micro-scale primary phases precipitated in the liquid, about 1–2 μm, was designated as *primary crystal*, and the nanoscale phases formed in the later solid state reaction as *secondary crystal*. Fig. 3a and b are the back-scattered electron image (BEI) of the SD near the free surface and substrate, respectively. Previous studies [14,15] reported that, in the BEI image, an amorphous phase exhibited a featureless morphology, which was significantly different from the adjacent crystalline region. In this study, the SD shows many featureless areas, as arrowed in Fig. 3, which were originally believed to be amorphous phases co-existing with primary
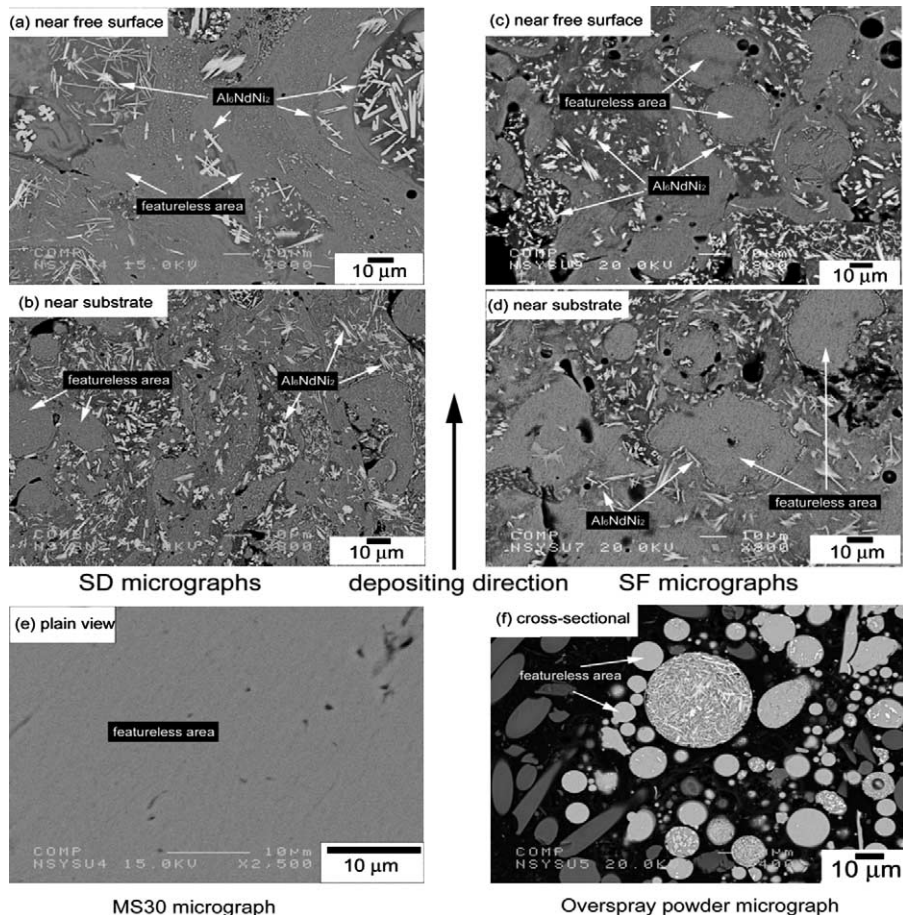

Fig. 3. Back-scattered electron images (BEI) of: SD near free surface (a) and near substrate (b); SF near free surface (c) and near substrate (d); MS30 (e); and overspray powders (f).
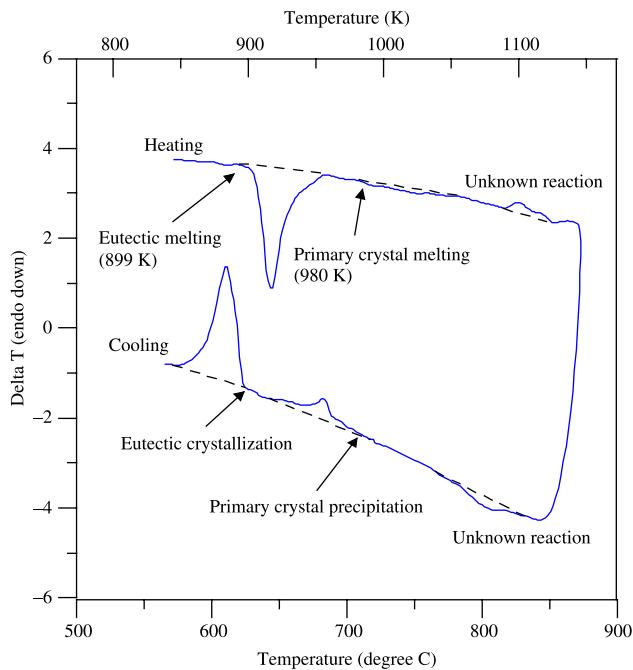
Fig. 4. DTA heating and cooling traces of the SF sample reveal the primary crystal precipitation and eutectic crystallization.

crystals. However, Fig. 2 shows that no exothermic peak in the DSC trace of the SD, implying that no retained amorphous phase exists. Therefore, the featureless areas in the SD would originally be the amorphous phase, which were completely devitrified to the secondary crystals during the spray forming process. Therefore, the SD is a bulk hybrid composite consisting of primary crystals and secondary crystals.

Fig. 3c and d are the BEI images of the SF near the free surface and substrate, respectively. The amorphous percentage in the SF was firstly estimated by conducting an image analysis on the BEI micrographs to be 55%, which is lower than the DSC result (63%). This is because the image analysis only considers the featureless area, but the other crystalline area may also contain amorphous phase. Fig. 1 shows multi-exothermic peaks for the SF, representing that amorphous devitrification did happen during heating in DSC. Therefore, SF is a bulk hybrid composite consisting of amorphous phases, primary crystals and secondary crystals.

Fig. 3e is the BEI image of the MS30. The micrograph shows the completely featureless area, representing a single amorphous phase. Fig. 3f shows the BEI image of the SP. The powder with a cross-sectional diameter less than 10 μm shows the completely featureless morphology, which implies that there is a critical size for the powder's amorphization.

To elucidate the primary crystals evolution in the SF, DTA heating and cooling traces were generated as in Fig. 4. Upon heating the SF, a eutectic melting occurred at about 899 K, at which all the α-Al crystals and some unknown phases melted into the liquid state. The melting of the residual primary crystals occurred in a wide temperature ranging from 980 to 1050 K, as shown in the heating trace. In the cooling trace, however, a sharp peak corresponding to primary crystal precipitation was present, occurring also at about 980 K. Therefore, the precipitation temperature of the primary crystal during solidification of the SF should be about 980 K.

4. Discussion

The primary crystals in the SD and SF are mostly of rod shape. The aspect ratio of primary crystals in the SD near the free surface (Fig. 3a) is significantly larger than that in the SD near substrate (Fig. 3b). This is because that the material near the substrate was forced-cooled by the LN constantly during the deposition, which retarded further growth of the primary crystals during spray forming. The aspect ratio of primary crystals in the SF (Fig. 3c and d) were similar to that in the SD. The compositions (at.%) of the primary crystals measured by the WDS technique were 72.5($\pm$2) for Al, 9.7($\pm$3) for Nd and 17.8($\pm$1) for Ni, so the primary crystal was determined to be Al_6NdNi_2. It's worth noting that no $Al_{11}Nd_3$ crystal was found
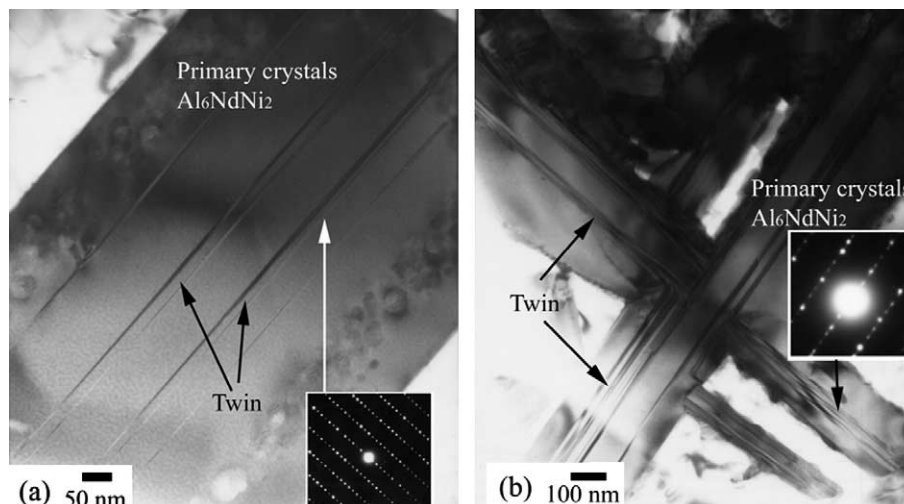

Fig. 5. TEM, bright field (BF) images and selected area diffraction patterns (SADPs) from the primary crystals (Al_6NdNi_2) observed in the SD and SF are shown in (a) and (b), respectively. Several parallel twins are found in the crystals. Zone axis=[110].
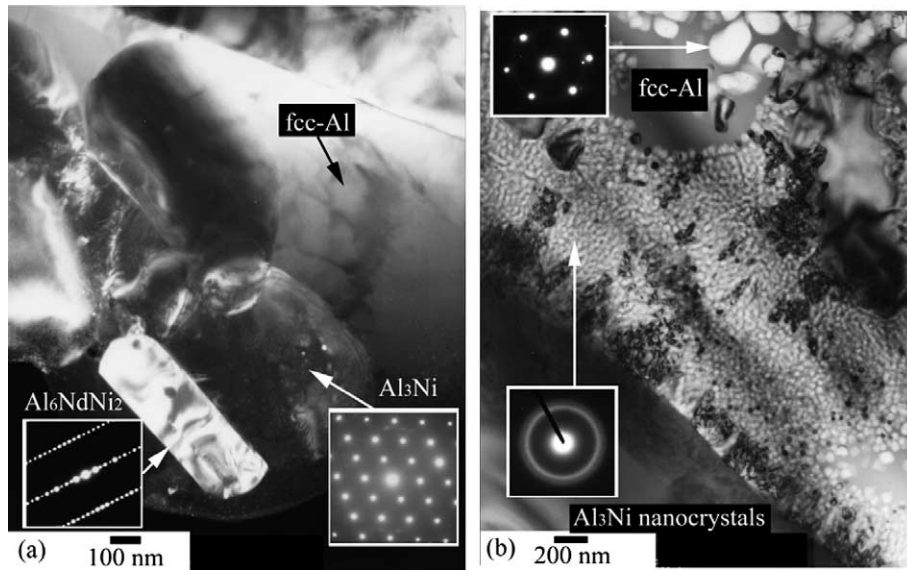
Fig. 6. TEM, BF images and SADPs from the secondary crystal (α-Al, Al_3Ni and Al_6NdNi_2) observed in the SD and SF are shown in (a) and (b), respectively. Zone axis = [110].

in the microstructure of SF, but a large amount of Al_6NdNi_2 crystals existed. Therefore, the XRD peaks of $Al_{11}Nd_3$-like in Fig. 2, for example the (101) and (130) peaks, should be the contribution of the Al_6NdNi_2. However, as no crystallography information is available for the Al_6NdNi_2 phase in the database [19], the confirmation of the X-ray peak requires further investigation.

Fig. 5 shows the TEM, bright field (BF) images of the primary crystals in the SD and SF. The compositions measured by the nanovolume EDS were $67.28 \pm 2\%$ Al, $10.8 \pm 1\%$ Nd and $22.02 \pm 1\%$ Ni, so the Al_6NdNi_2 phase was further confirmed.

Fig. 6 is the TEM, BF images of the secondary crystals (α-Al, Al_3Ni and Al_6NdNi_2) in the SD and SF. The nearly round-shaped α-Al crystals in the SD or SF (as arrowed) are

with the dimension of 200 nm. The size of the Al_6NdNi_2 secondary crystal, also 200 nm in width, is much smaller than that of the Al_6NdNi_2 primary crystal, 1–2 μm, shown in Fig. 3. Noted that the nanoscale Al_3Ni crystals in the SF, as arrowed in Fig. 6b, exhibit a near-amorphous ring pattern, which confirms that the featureless area consist of the secondary crystals embedded in the amorphous matrix. In comparison, the Al_3Ni crystals in the SD, as shown in Fig. 6a, exhibit a typical Al_3Ni pattern and with the dimension much larger than that in the SF.

Fig. 7a is the TEM, BF image and corresponding SADPs of the secondary crystals (α-Al, Al_3Ni, $Al_{11}Nd_3$ and Al_6NdNi_2) observed in the completely devitrified MS30. The atomic fractions of the phases were determined by the nanovolume EDS. The secondary crystals are similar in morphology and with the dimensions ranging from 200 to 300 nm, suggesting
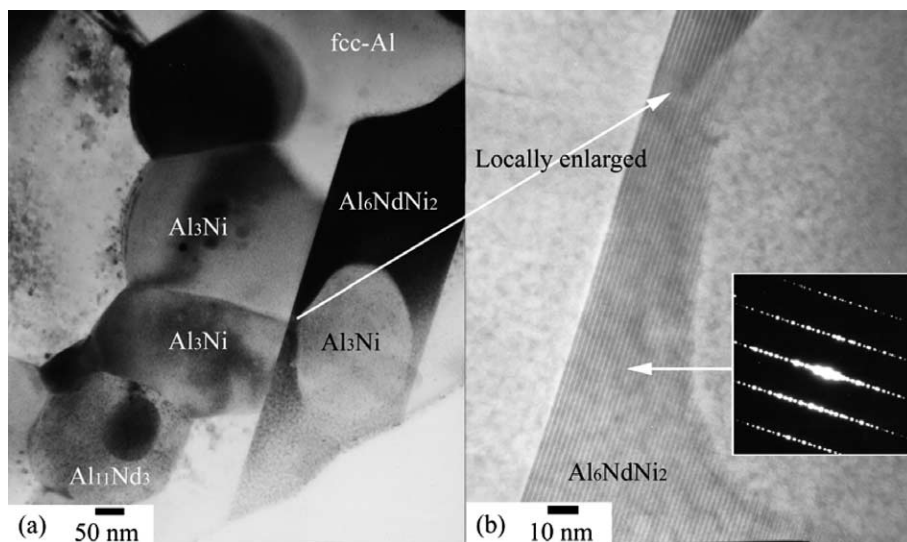

Fig. 7. TEM, BF image of the secondary crystals (α-Al, Al_3Ni, $Al_{11}Nd_3$ and Al_6NdNi_2) in the completely devitrified MS30 is shown in (a). The locally magnified high resolution image and the SADP in (b) reveal the layered structure of secondary Al_6NdNi_2 crystals. Zone axis = [110].

that they all grew up from solid state reaction in the amorphous matrix. Fig. 7b shows the locally enlarged high resolution image taken from Fig. 7a, which reveals the layered structure of Al_6NdNi_2 crystals. The SADP taken from the Al_6NdNi_2 secondary crystal in the MS30 is similar to the SADP of the Al_6NdNi_2 primary crystal in the SD, as shown in Fig. 5a. However, the calculated d-spacing (at zone axis [110] and direction [$1\bar{1}0$]) of the former is 1.7 nm, which is much larger than that of the later, 0.89 nm. The smaller d-spacing for the Al_6NdNi_2 primary crystal in SD specimen might be caused by the compressive effect generated by the deformation twins formed in the crystal, which were formed during spray forming.

During spray forming, the severe temperature gradients and the large stirring and impacting during droplets depositing, together with the mismatch of the thermal expansions between the primary crystals and adjacent amorphous matrix, were sufficiently large to trigger the formation of deformation twins in the primary crystals below glass transition temperature.

A great amount of deformation twins were surely observed in most of the primary crystals Al_6NdNi_2 in either the SF or SD, as shown in Fig. 5. It also shows a dendritic shaped primary crystal in the SF, in which the density of the deformation twins is larger than that in the SD. The selected area diffraction patterns (SADPs) taken from the primary crystals were also affected by the twins, especially that in the SF. The patterns are not uniformly diffracted and some dots at 1/3 and 2/3 separation are relatively weak, which are the characteristic features of the twins.

However, no deformation twins were found in the secondary crystals of the completely devitrified MS30, as shown in Fig. 7. This is because that there was no large stirring involved, and the CTE mismatch between the nanoscale secondary crystals and adjacent nanocrystalline matrix is much smaller.

5. Conclusions

1. The spray-formed $Al_{85}Nd_5Ni_{10}$ deposit is a bulk hybrid composite consisting of nanostructured phases, including Al_6NdNi_2 primary crystals and Al_3Ni, Al_6NdNi_2 secondary crystals, dispersed in the nanocrystalline α-Al matrix.
2. The spray-formed flake is a bulk hybrid composite consisting of 63% amorphous phase and 37% nanostructured phases, including Al_6NdNi_2 primary crystals and α-Al, Al_3Ni, Al_6NdNi_2 secondary crystals dispersed in the amorphous matrix.
3. The completely devitrified melt-spun ribbon is a hybrid composite consisting of α-Al, Al_3Ni, $Al_{11}Nd_3$, and

Al_6NdNi_2 secondary crystals with a dimensions of about 200–300 nm.
4. Deformation twins were observed in the Al_6NdNi_2 primary crystals in the SD and SF, which were produced during the growth of the primary crystals due to the large impacting and stirring during spray forming, and the thermal expansion coefficient mismatch between the primary crystal and adjacent amorphous phase.
5. No deformation twins were found in the Al_6NdNi_2 secondary crystals in the MS30, since there was no large stirring involved, and the CTE mismatch between the nanoscale secondary crystals and adjacent nanocrystalline matrix is much smaller.

References

[1] Shiflet GJ, He Y, Poon SJ. J Appl Phys 1988;64(12):6863.
[2] Chen LC, Spaepen F. Lett Nat 1988;336:366.
[3] Greer AL. Science 1994;267:1947.
[4] Inoue A, Kimura H. J Light Met 2001;1:31.
[5] Perepezko JH, Hebert RJ, Tong WS. Intermetallics 2002;10:34.
[6] Lu K. Mater Sci Eng R 1996;16:161.
[7] Inoue A. Prog Mater Sci 1998;43:365.
[8] Grant PS. Prog Mater Sci 1995;39(4–5):497.
[9] Su YH, Tsao CYA. Metall Mater Trans 1997;28B(12):1249.
[10] Chen YM, Su YH, Lin RW, Tsao CYA. Acta Mater 1998;46(3):1011.
[11] Guo MLT, Tsao CYA. Mater Sci Eng 2002;A326(1):1.
[12] Alan L. Met Powder Rep 1999;May:28.
[13] Oguchi M, Inoue A, Yamaguchi H, Masumoto T. J Mater Sci Lett 1991; 10:289.
[14] Afonso CRM, Bolfarini C, Kiminami CS, Bassim ND, Kaufman MJ, Amateau MF, et al. Scripta Mater 2001;44:1625.
[15] Afonso CRM, Bolfarini C, Kiminami CS, Bassim ND, Kaufman MJ, Amateau MF, et al. J Non Cryst Solids 2001;284:134.
[16] Inoue A. Mater Sci Eng 1994;A179/A180:649.
[17] Inoue A. Mater Sci Eng 1994;A179/A180:654.
[18] Gödecke T, Sun W, Lück R, Lu K. Z Metallkd 2001;92(7):717.
[19] Powder Diffraction File, The International Center for Diffraction Data, USA; 2004 release (sets 1–54 plus 65 plus 70–89).
[20] Sá Lisboa RD, Kiminami CS. J Non Cryst Solids 2002;304:36.
[21] Bassim N, Kiminami CS, Kaufman MJ. J Non Cryst Solids 2000;273:271.